Impact of Fuselage on Transition Location in the CRM-NLF Wing

Henrique Folgado Soares Amorim de Figueiredo
henrique.a.figueiredo@tecnico.ulisboa.pt

Instituto Superior Técnico, Lisboa, Portugal

October 2022

Abstract

The design of wings with extended laminar regions is a promising concept for the reduction of fuel consumption of aircraft. To achieve this, the computational tools used for the design of natural laminar flow wings need to mature. The purpose of this work is to extend our understanding of the transition process and its evaluation with Computational Fluid Dynamics (CFD). The Common Research Model for Natural Laminar Flow (CRM-NLF) transonic wind tunnel model is used for the study case as it provides valuable experimental data used for comparison. The model is evaluated with and without the inclusion of fuselage. The transition prediction determined by the DLR TAU-Code is evaluated and compared between both cases with the goal of understanding the effects of the fuselage on the predicted laminar extent. A set of hybrid computational meshes was developed for the isolated wing and wing-body model. Verification of wing solutions is performed with a grid refinement study. For the wing-body model the results were compared to available computational and experimental data. A stability analysis investigated the transition process and laminar extent for both configurations at different spanwise stations. The isolated wing showed a reduced laminar extent near the root, with the increase of cross-flow instabilities.
Keywords: CFD, natural laminar flow, CRM-NLF, transition, transonic

1. Introduction

Environmental concerns and the rise of gas prices have been catalysts for technologies with the potential to counteract them. With that objective in mind, the aviation industry over the years, has invested significant amounts of money on research for fuel saving technologies. A major contributor to a vehicle's overall drag is the skin friction drag. One of the techniques that has shown potential for the reduction of skin friction drag is the application of Natural Laminar Flow (NLF) airfoils with the objective of extending laminar flow on a wing.

The benefits of NLF technology are already known, but its application has been limited for a reason. For current aircraft design, most Computational Fluid Dynamics (CFD) simulations are carried out under the assumption of a fully turbulent flow field. That is a reasonable approximation for current aircraft, as most have been designed with that in mind. The extent of laminarity is also limited at transonic speeds due to the presence of a shock. However for NLF technology it is not useful to assume a fully turbulent flow field. It requires a set of more complex tools to accurately model the laminar region and its extension, along with the transition process. In addition to the difficulties in design, the manufacturing of NLF wings provides an added challenge due to the high sensibility of laminar flow. As such, best practices for surface finish and strict tolerances in manufacturing are mandatory.

In order to better design, the computational tools also need to be improved. That requires increasing amounts of research and experimental data to validate those cases. The data can either be obtained through flights or wind tunnel experiments.

A recent design that has showed the capabilities of NLF is the Common Research Model for Natural Laminar Flow (CRM-NLF) model [1], developed by NASA. NASA has also developed best practices for NLF testing in the National Transonic Facility (NTF) and has done so successfully. As such, the CRM-NLF is paired with a signifcant amount of experimental data which makes it a better study case than most other published NLF designs.

This work seeks to contribute to the understanding of these tools by applying them to the CRM-NLF model. The CFD Solver DLR TAU Code is applied to the CRM-NLF model to evaluate the impact of the fuselage on the predicted laminar ex-

tent on the wing. The prediction is executed by the TAU Transition Prediction Module composed of a boundary layer solver and linear stability code coupled with a e^N method.

2. Fundamentals

2.1. Governing Equations of The Flow

Fluid dynamics studies the behaviour of a fluid. The fluid is considered a continuum and its behaviour is determined by conservation and balance laws: conservation of mass, momentum and energy. For a certain flow quantity, this means that the total variation inside an arbitrary volume is expressed as the net effect of the fluxes across its boundaries, any internal sources and the internal and external forces acting on the volume [2].

The behaviour of a flow can be described by three conservation laws, that together form the Navier-Stokes system of equations. For a three-dimensional, compressible flow of a Newtonian fluid the equations take the form:

$$Continuity \qquad \frac{\partial \rho}{\partial t} + \vec{\nabla}.(\rho \vec{v}) = 0 \tag{1}$$

$$x, y, z\ Momentum \qquad \frac{\partial \vec{v}}{\partial t} + (\vec{v}.\vec{\nabla})\rho\vec{v} = -\vec{\nabla}p + \vec{\nabla}.(\mu\vec{\nabla}\vec{v}) + S_M \tag{2}$$

$$Energy \qquad \frac{\partial \rho\vec{v}}{\partial t} + (\vec{v}.\vec{\nabla})\rho\vec{v} = -\vec{\nabla}p + \vec{\nabla}.(\mu\vec{\nabla}\vec{v}) + S_M \tag{3}$$

The independent variables are the spatial coordinates x, y, z and the time coordinate t. There are six dependent variables: three velocity components u, v, z (for x, y, z directions, respectively) represented in the velocity vector $\vec{v}$, density ρ, temperature T (related to internal energy E) and pressure p.

The parameter μ is the dynamic viscosity, Φ is viscous dissipation, k is thermal conductivity and S_M and S_E are the momentum and energy source terms.

2.2. Boundary Layer

An idealised flow, where only the pressure forces count is called inviscid. There are no shear stresses on the surface of the body and as such, no viscosity. However, in a real flow these shear stresses exist near the body and generate a force that acts opposite to the flow's direction. For this situations, in a viscous flow, the flow velocity at a stationary body will be zero. This is called the no-slip condition. From this condition a velocity gradient will appear, giving rise to two different regions in the flow [3].

In the flow field away from the body, the velocity gradients are relatively small and viscosity has close to no effect. The flow is dominated by pressure forces and may be considered inviscid. However, close to the body, there will be a thin region with a velocity gradient normal to the surface. This is the boundary layer and it is dominated by viscous effects, as it was first noted by Prandtl in 1904 [3].

Depending on the flow regime, there are essentially two types of boundary layers: laminar and turbulent.

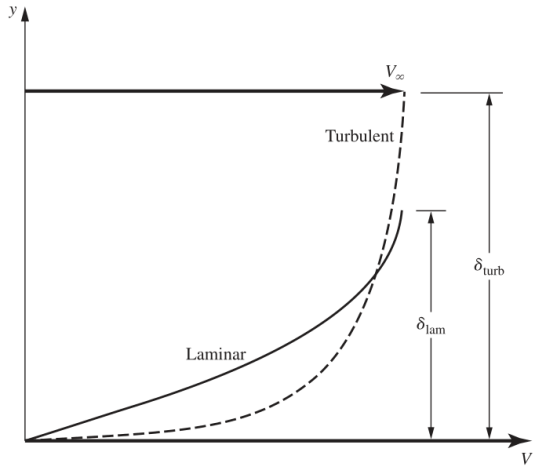

Figure 1: Velocity profiles of laminar and turbulent boundary layers [4].

Laminar and turbulent boundary layers will have different velocity profiles as can be shown in Fig. 1. The turbulent boundary layer typically has a larger thickness ($\delta_{turb} > \delta_{lam}$) and a higher velocity gradient at the wall. This leads to an increased shear stress at the wall and consequently higher viscous drag compared to the laminar boundary layer. This is one of the reasons behind the desire to extend the laminar region on a surface of the wing.

2.3. Transition Modelling

For a typical external flow around a body, the boundary layer will start laminar and as the Reynolds number increases, it eventually transitions to turbulent. This process is of great importance as it affects the characteristics of the boundary layer and consequently the forces acting on the body. Although the transition is a region with a finite length, it is typically assumed to happen suddenly at a transition point x_{crit} when the critical Reynolds number Re_{crit} is reached.

The transition depends then on the Reynolds number and pressure distribution of the outer flow, but also on the roughness of the wall and the level of disturbance of the outer flow (turbulence intensity) and is accompanied by a significant increase in boundary layer thickness and wall shear stress [3].

2.3.1 Transition on a Swept Wing

Transition is caused by the growth of instabilities in the boundary layer that eventually leads to a fully turbulent flow. For a swept back wing in a three-dimensional flow there are three main types of instabilities: Tollmien-Schlichting Instabilities (TSI), Cross-Flow Instabilities (CFI) and Attachment Line Instabilities (ALI). The TSI only occur downstream with the increase of the Reynolds number. So the first concern in avoiding transition in a swept wing will be the CFI and ALI.

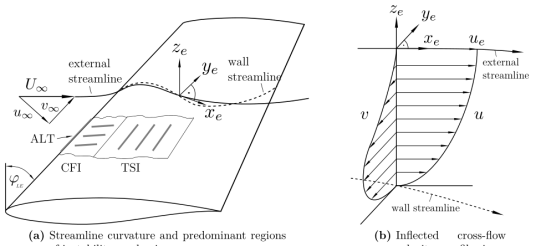

(a) Streamline curvature and predominant regions of instability mechanisms

(b) Inflected cross-flow velocity profile in a 3D boundary layer

Figure 2: Different types of instabilities on a swept wing and velocity profiles in the chordwise and spawnise directions, from [5].

2.3.2 Attachment-Line Instabilities

The attachment line is a line along the leading edge that separates the flow over the upper surface from the flow over the lower surface. Near the attachment line the flow is highly three-dimensional and has a high impact on the flow downstream. ALI become more prominent as the sweep angle increases.

2.3.3 Cross-Flow Instability

The superposition of CFI is intensified on swept wings. This is due to the additional pressure gradient along the wing and the fact that the boundary-layer then becomes three-dimensional. They are predominant near the leading edge (Fig. 2a) where the tangential component of the velocity is stronger.

For the cross-flow component of the profile, the boundary conditions are no-slip at the surface and zero velocity at the edge of the boundary layer. For a velocity profile of this kind, shown in Fig. 2b, with the velocity profile in the y direction, there is at least one inflection point, which means it will be very unstable at very low Reynolds numbers.

2.4. Linear Stability Theory

Linear Stability Theory (LST) attempts to explain the transition from laminar to turbulent boundary-layer. It assumes that the laminar flow is affected by small disturbances, that in the case of external flow, can come from irregularities in the flow or wall roughness. The main goal is to determine the indifference Reynolds number [3]. Below this number, the flow remains stable and all the perturbations are damped.

The unsteady disturbances can be superimposed onto the steady boundary-layer flow. For the considered flow, the coordinate system used will be x for the streamwise direction, y spanwise direction and z the direction perpendicular to the wall, with respective velocities u, v, w. A locally parallel flow is assumed for the boundary layer, which implies that the a given property q in a three-dimensional flow will depend only on z [6] and can be given as

$$q(x, y, z, t) = \bar{q}(z) + q'(x, y, z, t) \tag{4}$$

where letters with the bar (-) symbol are related to the base flow and the components with the prime symbol $'$ relate to the small disturbances. The variable q can be a velocity component (u, v, w), pressure p, density ρ or temperature T. The disturbances are typically assumed to take the form of a plane wave in the steady boundary flow [7], for which the the following *ansatz* applies

$$q'(x, y, z, t) = \hat{q} e^{\alpha x + \beta y - \omega t} \tag{5}$$

where $\hat{q}$ represents the complex amplitude of the wave and the exponential term, the harmonic characteristics. Regarding the parameters inside the exponential,

- α is the chordwise wavenumber,
- β is the spanwise wavenumber and
- ω the frequency.

The problem can be formulated in a temporal or spatial approach. For the temporal approach α and β are real numbers and ω is a complex number, while for the spatial approach α and β are complex numbers and ω is a real number [8].

2.4.1 e^N method

The e^N method is a semi-empirical criterion for which the stability characteristics of a boundary layer are analysed in terms of the growth rates of local disturbances. These amplification rates are then integrated to obtain the *N-factor*. As it is based on the linear stability theory, it is expected to work well in cases where the transition is dominated by the linear phase of breakdown [9].

The growth rates of the disturbances can be analysed using the local amplitude function A, derived from the physically relevant, real part, of equation 5. Using spatial theory for an incompressible and

two dimensional boundary layer, the amplification rate becomes:

$$\frac{1}{A}\frac{dA}{dx} = -\alpha_i. \tag{6}$$

The logarithmic amplification factor N is obtained when the characteristic growth rate of the disturbance α_i is integrated from the neutral point until a given location x. As such it can be written as:

$$N = ln\left(\frac{A}{A_0}\right) = ln\left(-\int_{x_0}^{x} \alpha_i dx\right), \tag{7}$$

where A and A_0 are the amplifications at a given location x and x_0 respectively.

The boundary layer equations can then be solved for a large number of stations x_i, using LST to obtain the growth rate of the disturbances. The curve that connects the maximum *N-factor* for each frequency is called the *N-factor* envelope.

The e^N method then assumes that transition occurs when a critical *N-factor*, N_{crit}, is reached. Obtaining the transition location experimentally for a set of cases, will provide a reference for the critical *N-factor* for which transition occurs.

3. Methodology

The base CRM-NLF model is provided by NASA [10]. Both a half-model wing-body configuration as well as an isolated wing configuration (fuselage removed) are considered. For the CFD simulations the configurations are set on a symmetry plane and the fluid domain is limited by a semi-sphere farfield with a radius corresponding to 100 times the semi-span. The hybrid computational meshes were generated using the commercial software Pointwise. On the surface of the wing, the reference meshes are defined with 300 points in the chordwise direction, for each surface of the wing, and 450 points in the spanwise direction. The surface mesh on the wing tip and fuselage (for the respective case) are unstructured. The boundary layer is resolved with a 100 structured layers nodes in the normal direction. The first cell height is based on the $y^+ = 0.35$ measured at 10% of the Mean Aerodynamic Chord (MAC). This leads to a first cell height of $7.73 \times 10^{-7} c_{med}$. A constant growth ratio of 1.104 in the normal direction was used for the structured layers. The rest of the fluid domain is unstructured. The final mesh for the wing-body configuration consists of approximately 27.6 Million points, while the mesh for the isolated wing has approximately 25.8 Million points.

The steady RANS simulations are executed using the DLR TAU code [11]. The Transition Prediction Module from the DLR TAU Code determines the transition. The module consists of the boundary-layer code COCO [12] for swept, tapered wings and the linear stability equations solver LILO [7]. The coupling between these tools follows the diagram represented in Fig. 3.

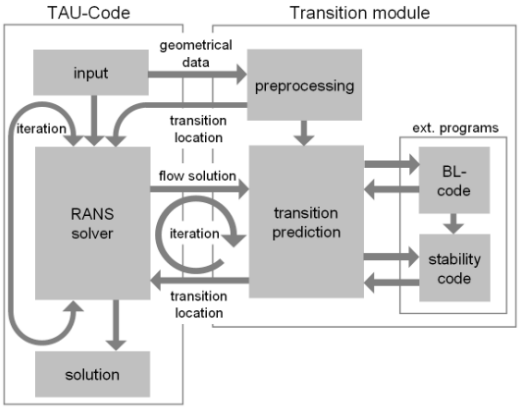

Figure 3: TAU COCO-LILO coupling [13].

Two different computations are executed for each case: a fully turbulent one and one using the transition prediction module. In the simulations with transition the upper surface of the wing is kept laminar until the transition location detected by the code and fully turbulent afterwards. The turbulence is modelled with the $k-\omega$ SST Menter model (1994). The turbulence intensity was set to 0.24% based on the levels of turbulence obtained for the NTF [14]. The lower surface is kept laminar up to $x/c = 5\%$, as reported by NASA for the experimental investigation of the CRM-NLF [15]. The transition module is executed at 23 different stations along the wing, including one at each of the rows that were used to extract wind tunnel data. The transition front is linearly interpolated in the regions between the stations. The applied transition criteria is the e^N method with a fixed critical N factor for TSI and CFI in an incompressible LST environement. The critical $N - factors$ were determined by [16] for the use of incompresssible LST with the CRM-NLF case and are 11.7 for TSI and 6 for CFI. The angle-of-attack α, Mach number M, Reynolds number based on the mean aerodynamic chord Re_{MAC} and the stagnation temperature T_{Total} are summarised in Table 1.

Table 1: Reference flow conditions

α [º]	Mach	$Re_{MAC}/10^6$	$T_{Total}[K]$
1.44848	0.856489	14.97197	277.108

4. Results

4.1. Isolated Wing

A mesh sensitivity study was performed to determine the mesh parameters. An iterative convergence study was carried out as well to ensure the steady state is obtained. For this mesh sensitivity study the wing is considered since the flow and the air-loads are the main focus. A mesh sensitivity study with the full configuration, wing and fuselage, would be more challenging due to increased complexity of the model. In particular, the region near the wing-body junction, with a concave angle, is prone to numerical errors and very sensitive to the quality of the mesh.

Three meshes for the CRM-NLF wing were generated, referred to as Coarse, Medium (reference) and Fine meshes presented in Table 2. These are hybrid meshes with structured mesh near the wall and unstructured mesh in the far field. The parameters for the created meshes are summarised in Table 2. In Table 2, Δ_s/c_{med} stands for the first cell height non-dimensionalised by the geometrical average chord (c_{med}) and GR stands for the Growth Ratio. The target y^+ is calculated at 10% of the Mean Aerodynamic Chord (MAC). The factor is calculated relative to the Medium mesh.

The CFD sensitivity was evaluated based on the aerodynamic loads, C_L and C_D. The transition location is also compared. The mesh sensitivity criteria, is to reach steady air-loads that are not depending on the mesh parameters. For this study if the change in the C_L is less than 1% of the medium mesh value, it is considered converged.

Table 3: Wing mesh convergence with fully turbulent simulations.

Configuration	C_L	C_D	**Nodes**
Coarse	0.2644	0.01074	13.1 M
Medium	0.2644	0.01071	25.8 M
Fine	0.2643	0.01068	50.9 M

For the turbulent simulations, the meshes show no significant variation of the C_L and C_D with increased refinement. The deviation of C_L and C_D compared to the Medium mesh is less than 1%. This indicates a good convergence and the reference medium mesh can be used without significant loss of accuracy, while keeping the computational costs considerably lower compared to the finer mesh.

The relatively small variation in C_D indicates that the viscous effects and specifically the logarithmic part of the turbulent boundary layer is being well captured. That means the y^+ has sufficiently low values on the wing surface. The fully turbulent simulations solve the averaged Navier-Stokes equations, and the boundary layer is achieved in the average sense. However, more important is to evaluate if the mesh is capable of resolving the laminar boundary layer. For example, to determine the laminar boundary layer profile a high number of cells normal to the surface is required inside the boundary layer. In addition, the Transition Prediction Module of the DLR TAU Code requires around 32-64 to sufficiently resolve the boundary layer features in COCO [17]. This target was set for the medium mesh by selecting an appropriate growth ratio of the cells.

Table 4: Wing mesh convergence with predicted transition.

Configuration	C_L	C_D	**Nodes**
Coarse	0.2951	0.01029	13.1 M
Medium	0.2951	0.01025	25.8 M
Fine	0.2951	0.01022	50.9 M

From Table 4 it can be seen that the C_L has converged and there is again only a small variation in C_D. The variation between meshes is not considered large enough (more than 1%) to justify the increased computational cost.

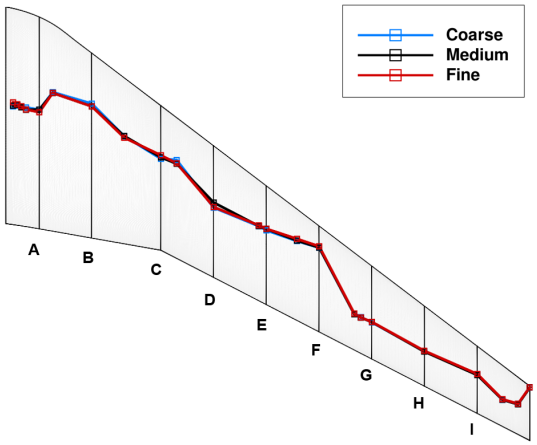

Figure 4: Laminar-to-turbulent transition location along the upper surface of the wing for the different obtained meshes; Blue for the coarse mesh, black for the medium mesh, red for the fine mesh.

Fig. 4 shows that all grids have a similar predicted transition, specially towards the wingtip. Compared to the Medium mesh, the results show a maximum deviation of 3.9% of the local chord for the Coarse mesh and 3.4% of the local chord for the Fine mesh, throughout all the stations. The coarse mesh shows an average deviation of 0.7% of the local chord, while the fine mesh shows an average variation of 0.8%, averaged over all the measured stations.

Table 2: Mesh parameters for each wing mesh.

Mesh	Nodes Chordwise	Nodes Spanwise	Nodes Normal	Nodes Total (M)	$\Delta s/c_{med}$	GR	y+	Factor
Coarse	238	357	79	13.1	9.74×10^{-7}	1.133	0.44	0.794
Medium	300	450	100	25.8	7.73×10^{-7}	1.104	0.35	1
Fine	378	567	126	50.9	6.13×10^{-7}	1.082	0.28	1.26

4.2. Comparison with Experimental and Computational Results

The addition of the fuselage alters the flow, especially near the root of the wing. As such, the wing-body configuration is evaluated and compared against available experimental and computational data. From now on, to distinguish between meshes, the wing-body mesh will be referred to as WBM, while the isolated wing will be referred to as WM. The WBM configuration is analysed in fully turbulent and with transition prediction (free transition mode).

Table 5: Comparison with experimental results and DLR simulation.

	Turbulent		Free Transition	
Results	C_L	C_D	C_L	C_D
EXP	-	-	0.312	0.0174
DLR	0.317	0.0172	0.352	0.0167
WBM	0.313	0.0175	0.351	0.0170

The obtained results for C_L and C_D are summarised in Table 5, along with the results obtained from wind tunnel measurements [18] and a RANS simulation of this case done by [19], at the DLR. The DLR simulation uses the TAU DLR-Code with the Transition Prediction module. It uses compressible LST with critical *N-factor=6* for both TSI and CFI. Table 6 shows the relative deviation from experimental results for the simulations.

Table 6: Deviation from experimental results.

	Turbulent		Free Transition	
Results	ΔC_L	ΔC_D	ΔC_L	ΔC_D
DLR	1.50%	-0.90%	12.9%	-3.80%
WBM	0.38%	0.57%	12.4%	-2.03%

Compared to the experimental data the turbulent simulations show a closer agreement than the free transition. In the case of the fully turbulent simulations, both fall within the uncertainty of $\delta C_L = 0.004$ reported for this case. Instead, for the C_D only the WBM falls within the reported uncertainty of $\delta C_D = 0.0001$ [20]. Regarding the free transition simulations both the DLR and WBM simulations show similar deviation to experimental data. The WBM shows 12.4% higher C_L and a 2.03% lower C_D compared to the experimental data. One reason contributing the differences in C_D is the existence of turbulence wedges in the experimental transition front that reduce the expected laminar area. There is also the possibility of the wind tunnel model being affected by aeroelastic effects not taken into account in the simulations. For the WBM, compared to the turbulent case, the free transition shows an increase in C_L of 0.038, or 12.1%, and a decrease in drag of 5.0 drag counts, or 2.9%.

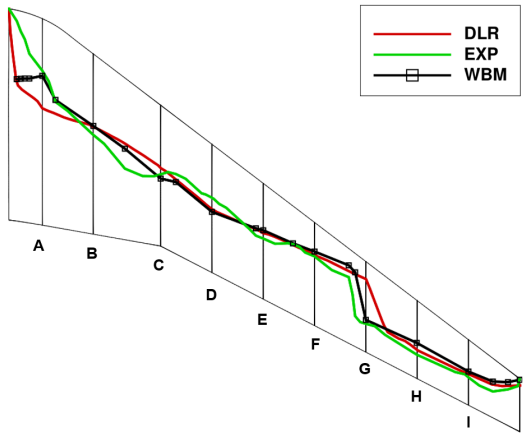

Figure 5: Laminar-to-turbulent transition location along the upper surface of the wing for the WBM simulation (black), the DLR simulation (red) and experimental location (green).

Regarding the transition fronts, shown in Fig. 5, both simulations are in agreement. The major differences arise towards the root of the wing and near Row G. The transition near Row G is very sensitive due to the presence of two shocks. The experimental transition front was extracted from [21], based on the Temperature Sensitive Paint images from [22]. The DLR front was extracted from [19].

4.3. Stability Analysis

The following section is dedicated to the evaluation of the transition fronts obtained for the WBM and WM. The compared transition fronts are showed in Fig. 6.

The analysis starts with the evaluation of the *N-*

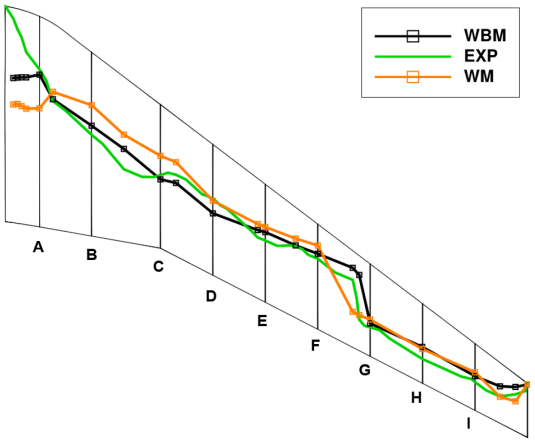

Figure 6: Laminar-to-turbulent transition location along the upper surface of the wing for the WBM simulation (black), the WM simulation (orange) and experimental location (green).

factor envelopes obtained with the WBM configuration at the nine different spanwise stations indicated in Fig. 6.

At the transition location it would be expected that the *N-factor* would reach the critical value for amplification of the respective instabilities. Fig. 7 shows that only rows A and H reach the critical values. For other rows, boundary layer separation was detected by the code COCO.

To seek understanding on the boundary layer separation causing transition, the velocity profiles obtained from COCO are analysed at Row B. The velocity profiles are presented as the non-dimensional height of the boundary layer $yd1$ as a function of the non-dimensional boundary layer velocity. For each case the velocity profile is shown at a set of fixed locations. Additionally the velocity profiles are shown at transition (marked TR) and for detected laminar boundary layer separation (marked SEP). Row B shows a transition location at approximately 40% of the local chord. Further investigation on the evolution of the boundary profiles shows that immediately after the transition a new inflection point appears in the cross-flow boundary profile (Fig. 8 (b)), indicating a change of direction of the flow near the wall. This can indicate boundary layer separation. Typically separation can be identified by observation of the skin friction coefficient C_f. When C_f becomes negative there is separation due to a change in the velocity direction. This criterion is only applicable for two-dimensional flows however. For three-dimensional flow separation, the solver would require a method to detect a limiting streamline leaving the wall. This example shows when boundary layer separation is detected in the cross-flow boundary layer even if it is not noticeable

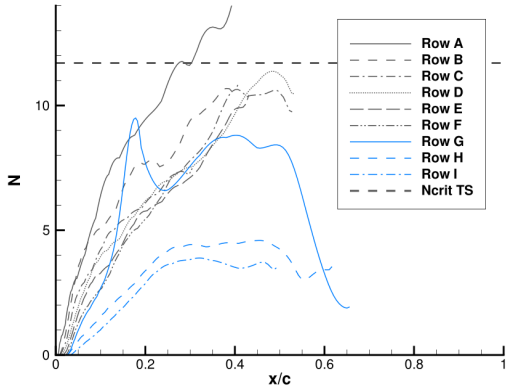

(a) TS

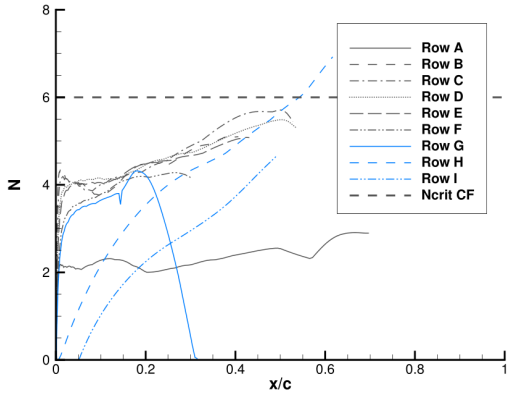

(b) CF

Figure 7: *N-factor* envelopes of the WBM at nine spanwise stations.

in the streamwise boundary layer (Fig. 8 (a)).

This analysis indicates the predominant influence of the cross flow on transition. Even in scenarios where the critical *N-factor* is not reached, the natural instability of the cross flow leads to detected separated flow regions, triggering the transition.

Similarly to the previous analysis, the growth of instabilities is evaluated for the isolated wing case.

For Row B the main cause of transition is now due to the growth of instabilities. Both TS and CF instabilities reach the critical level. The cross flow instabilities reach the critical *N-factor* sooner, resulting in the cross flow induced transition at 28.6% of the local chord (Fig. 9).

The transition location matches the velocity profiles shown in Fig. 10, with no detected separation. The current analysis shows less cross flow induced separation, however cross flow is still the main cause of transition due to the growth of instabilities. Further analysis with a full RANS boundary layer calculation to evaluate if the phenomena are physical

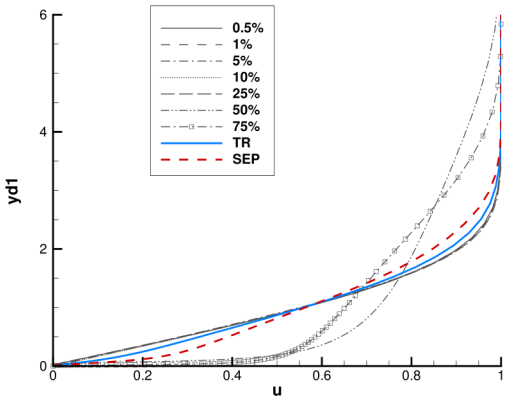

(a) Chordwise direction

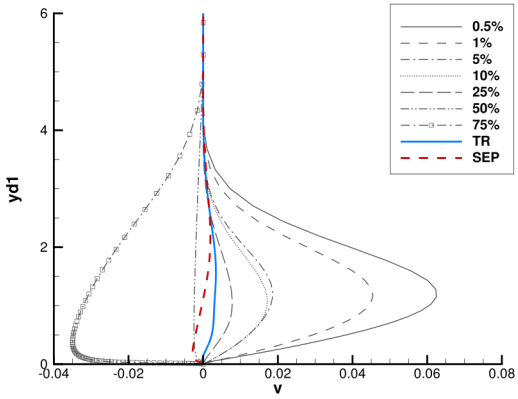

(b) Spanwise direction

Figure 8: Boundary layer velocity profiles for WBM at Row B.

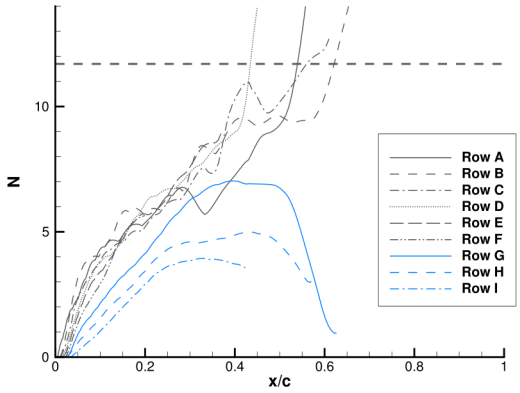

(a) TS

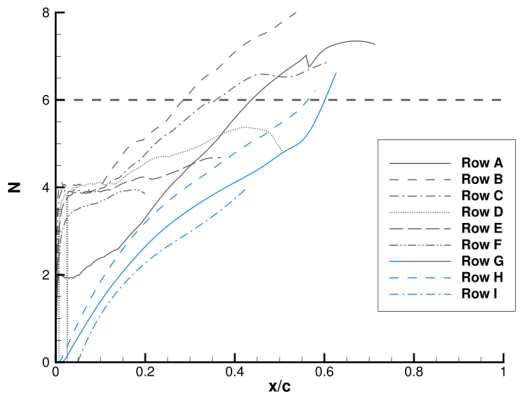

(b) CF

Figure 9: *N-factor* envelopes of the WM at nine spanwise stations.

and happening on the wing would be required to confirm this results. The code COCO, due to the conical flow approximation will not be accurate if there are dominant three-dimensional effects in the applied region. It is expected however, that the approximation produces reasonably accurate results in regions of the wing further away from the extremities. The use of RANS for a correct analysis of the cross-flow boundary layer has significantly higher costs however, with [17] recommending around 128 mesh points inside the laminar boundary layer to properly capture the cross flow effects. This has not been achieved with the current mesh.

A comparison between the WBM and WM configuration shows that the predicted transitions are similar on the outboard part of the wing, but get increasingly different closer to the root. An exception is the the region between Rows F and G, where a double shock is present. A difference in transition location was expected since the fuselage naturally alters the flow around the wing. However, it was not expected that the absence of fuselage would lead to a shorter laminar extent. The main difference in *N-factor* growth shows for Row B. The transition for the WM happens at 29% of the local chord while for the WBM it happens at 40%. The TSI have an increased growth rate for the WBM but do not lead to transition. The CFI start with a similar growth profile but after around 10% of the chord have an increased growth rate for the WM and end up causing transition.

At higher wavenumbers the CFI cause an earlier transition on the isolated wing case. CFI need to be stabilised by an accelerated flow near the leading edge. The pressure distributions (C_p) for both cases at Row B, Fig. 11, shows that the differences in C_p closer to the leading edge become more accentuated. In particular, the flow near the leading edge of Row B has an increased acceleration on the WBM, suggesting that the fuselage is accelerating the flow and contributing to the stabilization of CFI.

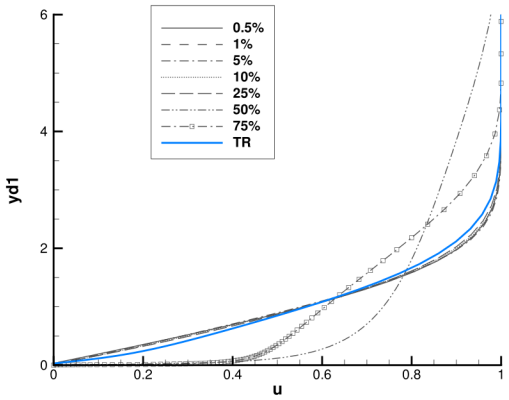

(a) Chordwise direction

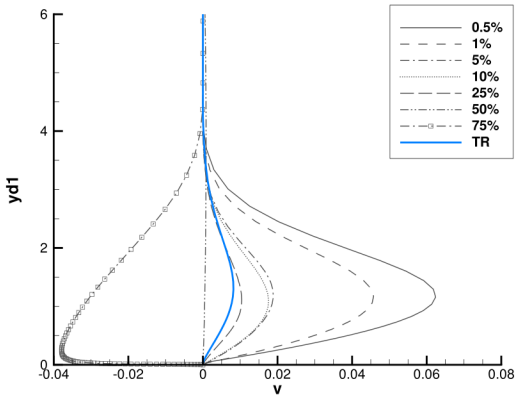

(b) Spanwise direction

Figure 10: Boundary layer velocity profiles for WM at Row B.

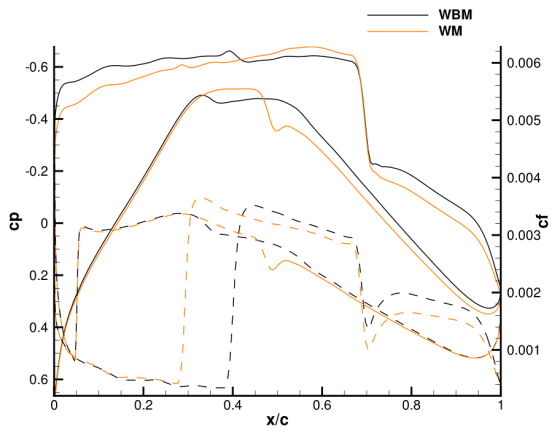

(a) Row B

Figure 11: Pressure distribution (solid) and skin friction (dashed) at Row B with transition prediction for the WBM (black) and the WM (orange).

5. Conclusions

A set of meshes was developed. Regarding the isolated wing mesh, the three levels of mesh refinement, coarse, medium and fine, showed similar results in terms of C_L, C_D and transition location. Regarding the wing-body simulations a good agreement between numerical simulations was shown. In particular the use of incompressible LST with a suitable critical *N-factor*, can provide similar results to a compressible LST approach. Compared to experimental results, the fully turbulent simulations showed a better agreement than the free transition. A few reasons are attributed to this. The experimental tests had turbulent wedges that affected the extended laminarity on the upper surface of the wing. As such, the C_D of CFD simulations would tend to be lower than the experimental. The delayed shock location when activating transition prediction leads to a higher C_L. It also affects the C_D, however not enough to compensate for the reduced viscous drag. Future investigations could help quantify the impact of the shock on the measured aerodynamic loads. Despite these differences the transition location for the wing-body configuration shows close agreement with experiment beyond 28% of the semi-span, demonstrating the capability of TAU for application in such cases.

Finally, a comparison between isolated wing and wing-body configurations showed that cross-flow instabilities were the main cause for transition. In particular the growth of these instabilities for the isolated wing case was more significant close to the root when compared to the wing-body configuration. For the isolated wing the flow does not have the required acceleration near the leading edge to dampen all the cross-flow modes.

Acknowledgements

This thesis was developed in collaboration with the Technical University of Braunschweig. Thank you to my supervisors Dr. Camli Badrya and Prof. João Sousa for the opportunity and support.

References

[1] Michelle N. Lynde and Richard L. Campbell. Computational design and analysis of a transonic natural laminar flow wing for a wind tunnel model. In *35th AIAA Applied Aerodynamics Conference*, 2017.

[2] J. Blazek. *Computational Fluid Dynamics: Principles and Applications*. Elsevier Science Ltd., Oxford, UK, 1st edition, 2001.

[3] H. Schlichting and K. Gersten. *Boundary-Layer Theory*. Springer-Verlag, Berlin Heidelberg, 9th edition, 2017.

[4] John Anderson. *Fundamentals of Aerodynamics*. McGraw-Hill Education, New York, NY, 6th edition, 2017.

[5] K. Risse. Preliminary overall aircraft design with hybrid laminar flow control. Master's thesis, RWTH Aachen University, 2016.

[6] D. Arnal. Boundary layer transition: Predictions based on linear theory. Technical report, NATO AGARD, 1994.

[7] G. Schrauf. *LILO 2.1 User's Guide and Tutorial*. GSSC Technical report 6, Bremen, Germany, 2006.

[8] J.M.M. Sousa and L.M.G. Silva. Transition prediction in infinite swept wings using navier–stokes computations and linear stability theory. *Computers and Structures*, 82:1551–1560, 2004.

[9] J. Sousa, N. Marques, and J. Pereira. Coupling navier-stokes calculations with linear stability analysis in wing design. In *VI Congresso Nacional de Mecânica Aplicada e Computacional*, 2000.

[10] CRM-NLF model geometry. https://commonresearchmodel.larc.nasa.gov/crm-nlf/crm-nlf-geometry/. Accessed 20 June 2022.

[11] DLR. *Technical Documentation of the DLR TAU-Code Release 2019.1.0*, 2019.

[12] G. Schrauf. *COCO A Program to Compute Velocity and Temperature Profiles for Local and Nonlocal Stability Ananlysis of Compressible, Conical Boundary Layers with Suction*. ZARM Technical report, 1998.

[13] Normann Krimmelbein and Andreas Krumbein. Automatic transition prediction for three-dimensional configurations with focus on industrial application. In *40th Fluid Dynamics Conference and Exhibit*, 2010.

[14] Jeffrey Crouch, Mary Sutanto, David Witkowski, A. Watkins, Melissa Rivers, and Richard Campbell. Assessment of the national transonic facility for natural laminar flow testing. In *48th AIAA Aerospace Sciences Meeting Including the New Horizons Forum and Aerospace Exposition*, 2010.

[15] General information on the CRM-NLF wind tunnel test. https://commonresearchmodel.larc.nasa.gov/wp-content/uploads/sites/7/2019/09/CRM-NLF_Info.pdf. Accessed 15 Oct 2022.

[16] Normann Krimmelbein and Andreas Krumbein. Determination of critical n-factors for the crm-nlf wing. In Andreas Dillmann, Gerd Heller, Ewald Krämer, and Claus Wagner, editors, *New Results in Numerical and Experimental Fluid Mechanics XIII*, pages 195–204. Springer International Publishing, 2021.

[17] N. Krimmelbein. *TAU Transition module (V9.30)*. Institute of Aerodynamics and Flow Technology, DLR, 2015.

[18] Force and moment data for the CRM-NLF. https://commonresearchmodel.larc.nasa.gov/wp-content/uploads/sites/7/2020/09/CRM-NLF_NTF_Data_v3.xlsx/. Accessed 15 Oct 2022.

[19] Sebastian Helm, Michael Fehrs, Normann Krimmelbein, and Andreas Krumbein. Transition prediction and analysis of the crm-nlf wing with the dlr tau code. In Andreas Dillmann, Gerd Heller, Ewald Krämer, and Claus Wagner, editors, *New Results in Numerical and Experimental Fluid Mechanics XIII*, pages 185–194, Cham, 2021. Springer International Publishing.

[20] Melissa B. Rivers, Michelle N. Lynde, Richard L. Campbell, Sally A. Viken, David T. Chan, Anthony N. Watkins, and Scott L. Goodliff. Experimental investigation of the nasa common research model with a natural laminar flow wing in the nasa langley national transonic facility. In *AIAA Scitech 2019 Forum*, 2019.

[21] Michelle N. Lynde, Richard L. Campbell, and Sally A. Viken. Additional findings from the common research model natural laminar flow wind tunnel test. In *AIAA Aviation 2019 Forum*, 2019.

[22] Neal Watkins, Kyle Z. Goodman, and Sarah Peak. Transition detection at cryogenic temperatures using a carbon-based resistive heating layer coupled with temperature sensitive paint. In *AIAA Scitech 2019 Forum*, 2019.